

## Analytical crack growth in unidirectional composite flywheel

Lluís Ripoll<sup>\*1</sup>, José L. Pérez-Aparicio<sup>2a</sup>, Pere Maimí<sup>1b</sup> and Emilio V. González<sup>1c</sup>

<sup>1</sup>Mechanical Engineering & Industrial Construction, Universitat de Girona, 17003 Girona, Spain

<sup>2</sup>Continuum Mechanics & Theory of Structures, Universitat Politècnica de València, 46022 Valencia, Spain

(Received March 9, 2023, Revised March 29, 2023, Accepted March 30, 2023)

**Abstract.** Scarce research has been published on crack propagation fracture of flywheels manufactured with carbon fiber-reinforced polymers. The present work deals with a calculation method to determine the conditions for which a crack propagates in the axial direction of the flywheel. The assumptions are: flywheels made with just a single thick ply or ply clustering laminates, oriented following the hoop direction; a single crack is analyzed in the plane defined by the hoop and axial directions; the crack starts close to one of the free edges; its axial length is initially large enough so that its tip is far away from that free edge, and the crack expands the entire circumferential perimeter and keeps its concentric position. The developed method provides information for a good design of flywheels. It is concluded that a fracture-based crack propagation criterion generally occurs at a lower speed than a stress-based criterion. Also, that the evolution of failure with thickness using the fracture criterion is exponential, demonstrating that thin flywheels are relatively not sensitive to crack propagation, whereas thick ones are very prone.

**Keywords:** analytical stress analysis; composite material flywheel; crack growth; failure criteria; finite elements; linear fracture mechanics

---

### 1. Introduction

Composite flywheels are one of the few common applications of advanced composites for which the directionality of the fibers is more or less uniform and the thickness very high. Compared with metal parts, they have been increasingly used in many technological sectors due to their low weight and high traction resistance, which allow elevated angular velocities  $\omega$  and produce a good energy density.

A composite flywheel can be a long cylinder with several layers of different materials. However, in this article, we will study a single and thick layer for simplicity and for being widely used. Cylinders of several layers would behave similarly, but the governing equations are more complex. The rest of the parts, which are generally metallic: hub, center cup, spokes, endcaps, etc., are not included in the present analysis. The flywheel that rotates at  $\omega$  is under several tensile

---

\*Corresponding author, Professor, E-mail: lluis.ripoll@udg.edu

<sup>a</sup>Professor, E-mail: jopeap@mes.upv.es

<sup>b</sup>Professor, E-mail: pere.maimi@udg.edu

<sup>c</sup>Professor, E-mail: emilio.gonzalez@udg.edu

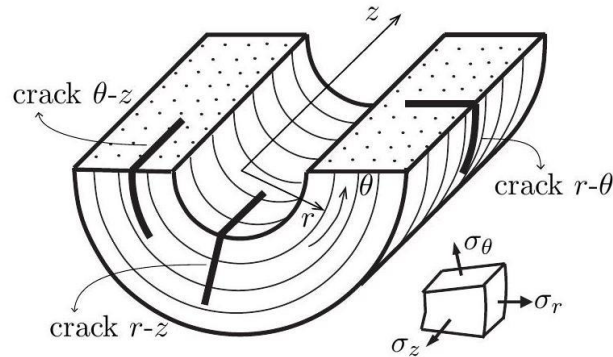


Fig. 1 Possible cracks in composite flywheel cut in half; cylindrical coordinates and stresses in differential element

stresses function of the centrifugal force  $f_i$  that is volumetric.

During operation, a possible cause for the start of a fracture would be the presence of microcracks generated through the winding process Koch *et al.* (2018): small air cavities can be created when the filaments and the matrix are deposited and cured. Any other material, manufacturing, transportation, etc. defect, would also be a crack initiator, and the inherent vibration of these machines often provokes the start and propagation of macrocracks.

For constant  $\omega$ , when an existing crack of variable length  $a$  propagates, it will be under a fracture mode similar to I, and its orientation is probably forced to be parallel to the direction of the fibers. In general, for a unidirectional laminate in the circumferential  $\theta$  (hoop) direction, the crack will be contained in one of the three orthogonal planes sketched in Fig. 1:  $r - z$ ,  $\theta - z$  or  $r - \theta$ , Lenz *et al.* (2014), Tzeng *et al.* (2006), Tzeng (1998). In thick-wall cylinders, the first propagation plane is unlikely since it requires the breakage of fibers; of the other two involving matrix breakage, the weakest will depend on the state of stress, see the following sections for disambiguation.

Under steady state regime, the highest mechanical component is the hoop or circumferential stress  $\sigma_\theta$ , as sketched in the detail of Fig. 1. The orientation of this component coincides with that of the fibers, the direction for which the longitudinal tensile strength  $X_{\theta+}$  is highest (Figs. 2(c), 2(d)); this coincidence makes composite flywheels one of the most efficient thick composite parts.

Suppose the hub is designed with sufficient elasticity to avoid pressing the composite cylinder through operation due to boundary conditions. In that case, the radial stress  $\sigma_r$  is null at the external  $r_e$  and internal  $r_i$  radii (Fig. 3). This stress increases in the bulk and reaches its maximum near the radial center. Also,  $\sigma_r$  is always much lower than  $\sigma_\theta$ ; still, it is very damaging since it acts in the plane perpendicular to the fibers, for which the transversal tensile strength  $X_{r+}$  is in CFRP typically 25 times lower than  $X_{\theta+}$ . Only for very thin-walled flywheels would  $\sigma_\theta$  be more damaging than  $\sigma_r$ .

The axial stress  $\sigma_z$  only appears when the length of the flywheel is significant concerning the other dimensions. Its value is often much lower or lower than the previous two, and its influence on failure is generally small: this low value makes the progression of the crack  $r - \theta$  unlikely. Notice that the distribution of  $\sigma_z$  must be self-equilibrating since no external axial loads exist in the axial direction, and no end caps are considered (Fig. 2(b)).

Stresses caused by sources other than the centrifugal force may be present under special

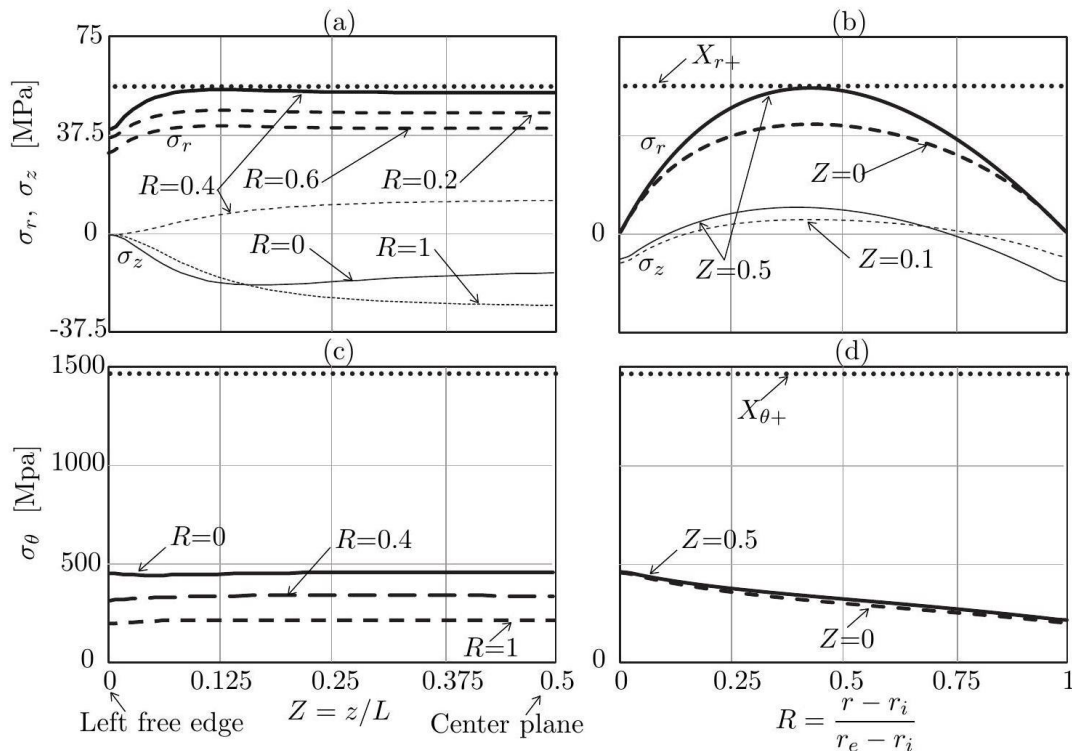


Fig. 2 (a), (c): FEM stresses for several radii along the first semilength of the cylinder. (b), (d): FEM stresses for three axial positions along the radius of the cylinder. Longitudinal and transversal strengths in [MPa]; in top figures, thick lines for  $\sigma_r$ , thin ones for  $\sigma_z$

conditions; for example, if the rotation speed varies in a short time (strong acceleration/deceleration), significant shear stresses appear in the circumferential plane Pérez-Aparicio and Ripoll (2011). Residual stresses may exist Koch *et al.* (2018), Tzeng and Pipes (1992), for example, due to manufacturing using the interference union of two cylinders or by moisture absorption. Still, they are usually only about 10% of the centrifugal ones; see Tzeng and Moy (2008), Arnold *et al.* (2002).

Only a little research has been published on composite flywheel fracture. The reference Lenz *et al.* (2014) designed a test program with the help of finite element analysis; Koch *et al.* (2018), Arnold *et al.* (2002), Wang *et al.* (2018) evaluated cycle life with other methods than fracture, such as micromechanics or damage models.

Some articles have studied crack growth in axisymmetric composite parts; for instance, Wang *et al.* (2020) carried out a dynamic fracture experiment of a plastic PMMA disk using an experimental digital laser dynamic caustic system. A discrete lattice spring method was used to simulate the crack growth, although the plastic was not reinforced with fiber. Investigations on mode-I fracture and thick composites were thoroughly carried out in El-Hajjar and Haj-Ali (2005) to assess the effect of material orthotropy in continuous filament layers with E-glass fiber and polyester matrix. Finally, the same authors developed in Haj-Ali *et al.* (2006) a cohesive finite element method for mode-I and -II crack growth analysis of thick-section composites and also for single-edge-notch specimens.

There are publications on different approaches to model fracture; in particular, Nguyen *et al.* (2022), Suljevic *et al.* (2022), Ibrahimbegovic and Mejia-Nava (2021), Ibrahimbegovic *et al.* (2022) studied viscoplastic, plasticity, damping, and multiple scales respectively. These works differ from the present since they are theoretical and very advanced. In the same journal, Rizov (2020) published a more practical work for analytical investigations of crack growth in tapered beams.

In the present study, a calculation method is derived to determine the conditions for which a crack propagates in the axial direction of the flywheel. For an absolute prediction, it would be necessary to carry out more complex studies, for example, the analysis of local phenomena and the priority of propagation along the direction of the fibers Cepero *et al.* (2019).

## 2. Preliminary case without crack

For a cylindrical and intact CFRP axisymmetric flywheel rotating at 48,000 [rpm], Fig. 2 show the stress distributions obtained with the Finite Element Method (FEM). The axisymmetric, transversally isotropic element of the research code FEAP Taylor and Govindjee (2020) was used; a mesh of about 3,400 square elements represented a rectangular section dimensioned by  $r_i = 0.1$ ,  $r_e = 0.2$  and  $L = 0.4$  [m]. The prescribed natural conditions were distributed forces, mimicking the centrifugal forces. The only essential boundary conditions necessary to enforce axial symmetry are in the middle vertical plane  $r - \theta$  defined by  $z = L/2$ . Although these FEM results are not directly the objective of the present work, they are presented to help the understanding of the fracture mechanics hypotheses and methodology and the interpretation of final results.

Along with the other properties, the values of the longitudinal  $X_{\theta+}$  and transversal  $X_{r+}$  strengths are listed in Table 1 and plotted as horizontal dotted lines in all Fig. 2 to assess their influence on failure. It is observed that the most damaging component is  $\sigma_r$  since its maximum practically coincides with the limit  $X_{r+}$  (Fig. 2(a), 2(b)). The hoop stress  $\sigma_\theta$  is about one-third of  $X_{\theta+}$  (Fig. 2(c), 2(d)), and the axial stress  $X_{r+}$  one-fourth (Fig. 2(a), 2(b)); finally, the three shear stresses are negligible.

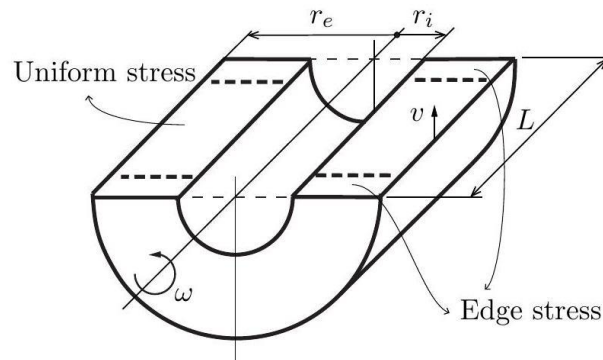
Fig. 2(c) also shows that  $\sigma_\theta$  is practically constant in  $z$ , and so is  $\sigma_r$  (Fig. 2(a)) except for a sharp decrease close to the free end; axial stresses are also almost constant with  $z$  outside the edges and in any case smaller than  $\sigma_r$ . Therefore, it can be considered that the stresses are independent of the axial position in the internal zones of the flywheel.

Clearly, there is an edge effect, but with the particularity that in it, the most damaging  $\sigma_r$  is lower than in the internal zones; shear stresses  $\tau_{r\theta}$ ,  $\tau_{rz}$  are also generated but under steady state of meager value. The physical reason for this decrease is that the confinement is less severe at and close to the axial ends, allowing some free deformations that cannot exist inside and relieving the material from part of the stresses (a plane stress condition). This edge effect differs significantly from flat laminated composites with fibers cut at the edges and placed in different directions. In the present types of flywheels, the fibers are not interrupted at the edge since their direction is always parallel to it. In conclusion, the edge effect is favorable in the particular case of the present flywheels.

The stress distributions of the figures confirm one of the ideas explained in the previous section: the tensile  $\sigma_r$  is the most damaging for thick unidirectional flywheels. Most published articles aim to find designs that decrease its effect on failure Wang *et al.* (2018), Ha *et al.* (2001),

Table 1 Material properties for a unidirectional Carbon Fiber Reinforced Polymer from González *et al.* (2018)

Property	Symbol	Unit	Value
Density	$\rho$	[kg/m <sup>3</sup> ]	1510
Elastic Modulus	$E_\theta$	[GPa]	116.7
-"-	$E_r$	[GPa]	8.3
Poisson ratio	$\nu_{\theta r}$	[-]	0.26
-"-	$\nu_{r z}$	[-]	0.52
Strength	$X_{\theta+}$	[MPa]	1477
-"-	$X_{r+}$	[MPa]	55.5
Fracture Toughness	$G_{\theta+}$	[kN/m]	248.5
-"-	$G_{r+}$	[kN/m]	0.62

Fig. 3 Axial zones according to stress distributions for a cylindrical flywheel. Angular  $\omega$  and peripheral linear  $v$  velocities

for instance, by intercalating different materials and/or thin elastic layers. Therefore, it can be expected that the fracture in the  $\theta - z$  plane of Fig. 1 is probable, or at least it should be studied in detail.

Since the present cylinder is “long”  $L > r_e - r_i$ , two very different zones can be differentiated considering the stress state; see Fig 3. In the two end zones, the edge effects cause a perturbation of the stresses, making them vary with  $z$ ; in the central zone called “uniform”, all stresses are practically constant in  $z$ . This uniform zone will be under generalized plane strain, with uniform axial deformation (see Pérez-Aparicio and Ripoll (2011) for justification).

Then, the central zone is more vulnerable to crack propagation, and therefore, its real fracture strength (not the nominal from testing specimens, see the next section) is relatively low.

### 3. Crack limitation in the $\theta - z$ plane

The fracture in the plane  $\theta - z$  is of mode I type, with a crack front similar to that of the normalized DCB (Iso15024) test for composite materials, but the distant zone behaves differently. In the workshop specimen, the point forces  $F$  separate the ends of the two arms without limitation; the large opening  $C$  or the maximum distance between the two separated arms increases through

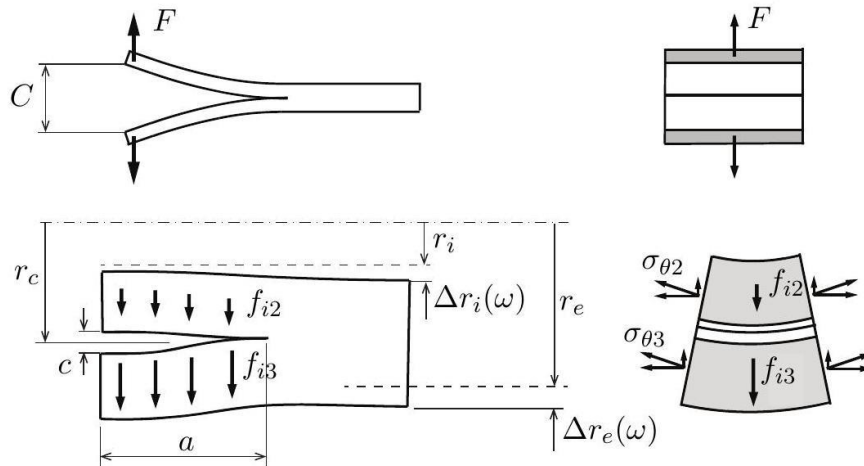


Fig. 4 Crack separation: top, unrestricted in a DCB specimen for composite materials; bottom, limited by adjacent material in a flywheel. For the latter, inertial forces differ in both sub-cylinders

the experiment. This opening is due to bending and only depends on the crack length, as shown in Fig. 4 top. But in a cylinder, the I-mode crack growth in the  $\theta - z$  plane of Fig. 4 bottom (a  $\theta - z$  cut for the crack of Fig. 1) is different: the smaller opening  $c$  is limited by the rest of the thick flywheel volume. Therefore, the two subcylinders are restricted to opening freely. In addition, the radial projection of the circumferential stress  $\sigma_\theta$  partially compensates for the centrifugal forces, and consequently, the opening is smaller. This behavior allows the analytical calculation of energies before and after the crack opening and, therefore, that of the dissipated energy.

The new internal, free surface created by the crack located by the radius  $r_c$  and defined by the length  $a$  modifies the distribution of  $\sigma_r$ . Subsequently, the inner and outer new subcylinders must reach a new equilibrium position with  $f_i$ .

This phenomenon can be appreciated in Fig. 5 frontal view: a differential element located at a point where the crack will start is subjected to  $f_i$ . As in the left figure, these forces must be compensated by the projections of sigma sub theta and by the differential d sigma sub r. When the crack is partially circumferential (center figure), the stress state is complex but non-necessary for the present model. Once the crack reaches the entire perimeter (right figure), it is possible to study the stress distribution as in Pérez-Aparicio and Ripoll (2011). In particular, at the differential element located at the same position (just outside  $r_c$ ), the stress  $\sigma_r$  disappears due to the boundary condition of a free surface, causing the outer cylinder to move outwards. Then, the hoop stress must increase to  $\sigma'_\theta$ , so the element remains in equilibrium for the same  $f_i$ . A similar situation occurs in the inner cylinder but moving inwards. Both movements generate a crack of limited opening  $c$ , much smaller than the DCB specimen for the same material.

#### 4. Geometry of fracture

In the intact cylinder of Fig. 3, we have differentiated between the axial external end zones (edge) and the internal one, where the stresses are almost uniform.

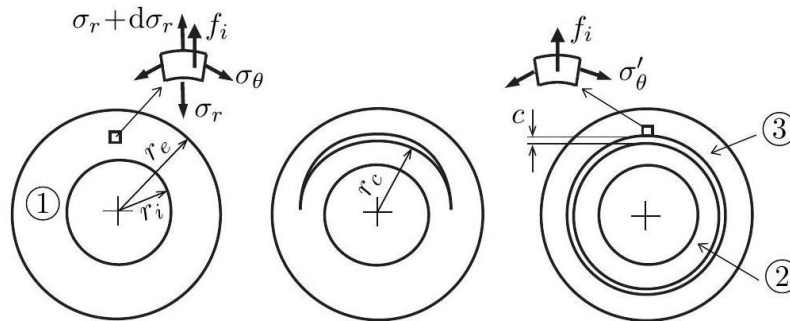


Fig. 5 Flywheel frontal view. Left: no crack and internal stresses of a differential element; central: partial crack; right: total crack and new stress state of the element at the same position

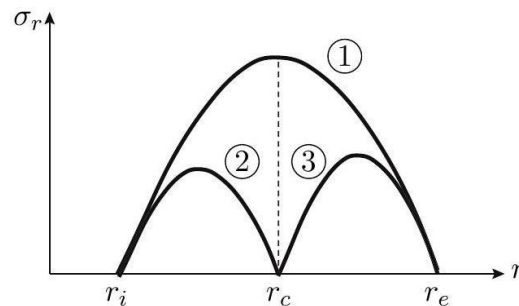


Fig. 6 Radial stresses at a generic section  $z$ -constant before (top parabola) and after the crack appearance (lower twin parabolas)

As justified before, a single crack in the  $\theta - z$  plane will be analyzed; we assume that this crack started close to one of the free edges and its length  $a$  is already large enough for its tip to be far away from that edge. It is also assumed that the crack expands the entire circumferential perimeter (Fig. 5 right) and keeps its concentric position; that is, it is axisymmetric. This hypothesis will allow us to use a relatively simple two-dimensional model similar to other published studies Tzeng (1998). In any case, a partial crack of the Fig. 5 center type will rapidly progress along the circumference since the tensile  $\sigma_r$  provokes a mode I opening against the commonly low fracture toughness  $G_{r+}$ , see Table 1. In addition, the axisymmetric premise sets a lower bound for failure; therefore, the present is a safe design procedure.

Since the current flywheel is made out of a single material, the crack is located near the radius  $r_c$ , approximately the median  $(r_e + r_i)/2$  where  $\sigma_r$  is maximum, see the distribution (1) in Fig. 6 for an intact cylinder. Once the crack appears,  $\sigma_r$  is nil at  $r_c$ , and its maximum is reduced to the center of both split cylinders (2) and (3). For a flywheel made out of several materials (case not studied here), the position of the maximum  $\sigma_r$  would depend on the relative radii and stiffnesses of the layers, as explained, for instance, in Ha *et al.* (2001).

In Fig. 7, three short subcylinders with constant stresses (uniform as in Fig. 3) can be distinguished: the intact one (1) and the “split” (2) and (3). At the edges of the flywheel, the stress state is still non-uniform. Around the crack tip, an axial transition zone between the uniform zones will exist; the stresses are again challenging to calculate in this transition. But the stresses for the two split cylinders can be calculated analytically with the formulae of Pérez-Aparicio and Ripoll

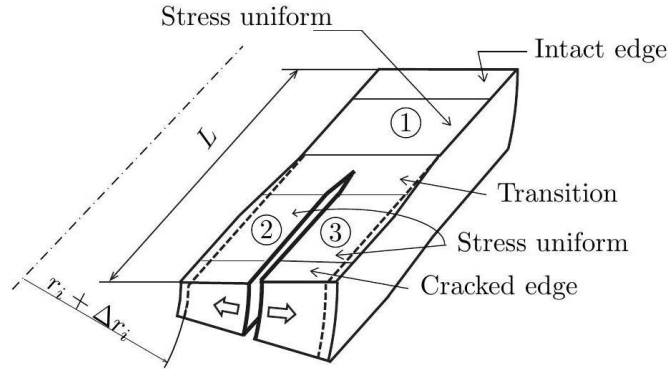


Fig. 7 Crack  $\theta - z$  divides part of the flywheel into two subcylinders. Stress-uniform zones (1), (2), (3) for stress and fracture. A dotted line near the free edge denotes the initial configuration, a continuous line deformed

(2003), considering the new  $r_i$  and  $r_e$ . For (1), the calculation is direct with the original external and internal radii.

## 5. Crack propagation

The crack growth study for a fixed  $\omega$  is based on a virtual advance (differential distance) of its front. While the cylinders (2) and (3) increase their axial length  $dz$ , (1) decreases the same amount, see Fig. 8 right. Then, this advance will cause a change of relative volumes, and since  $f_i$  is constant for a given  $r$  in the uniform zones, a perturbation of the displacement field appears, modifying the stress state. These changes imply an increment/decrement of internal energy  $\Delta U$ . Additionally, the change of displacement will generate work  $\Delta W$  of the centrifugal forces.

In this process, the volumes under a complex stress state, the cracked and intact edges (Fig. 7), or the transition zone simply translate and do not change (Fig. 8). Therefore, they should not be included in the calculations. This simplification is an essential advantage of the present formulation since both  $\Delta U$  and  $\Delta W$  are only non-zero in the volumes of the three stress-uniform cylinders of Fig. 7, allowing the obtaining of a closed-form solution.

The energies will be calculated from the radial displacement  $\Delta r(\omega)$ , denoted by  $u$  in what follows. At any point in (2), the increment of displacement is negative  $-\Delta u_2$  since once the crack appears, the radial displacement inside this internal cylinder is still positive (outwards in the direction of  $r$ ) but lower than what used to be at this point before the crack. The physical reason for this negative sign is that from a positive value,  $\sigma_r$  becomes zero; therefore, the cylinder (2) returns to its initial position. At the same time and free from the retention, the external cylinder (3) moves outside. In the outer (3), any point will have a positive  $+\Delta u_3$  since there is less internal mass to restrain it--see Fig. 8 for the drawing of both increments--. The radial displacements of any point of study and the intact cylinder (before the crack appears) can be calculated in (1) using the radii of the given point.

To simplify the calculation, it is considered that the centrifugal force of any point does not vary during the separation of the sub-cylinders, even if this point is under a slight increase of its radius due to the radial displacement. This hypothesis is common in published studies, for instance,

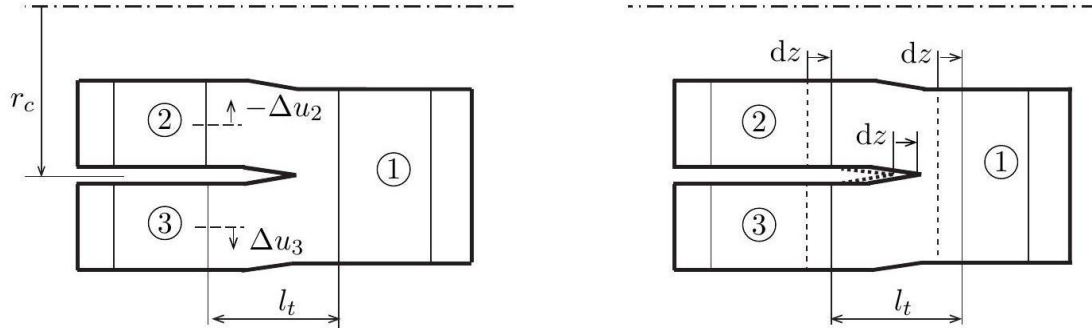


Fig. 8 Left: radial displacement of the two subcylinders formed by the axial crack. Right: crack length increment and related length change of stress-uniform zones (1), (2), (3). Length  $l_t$  of the transition zone does not change with  $dz$

Arnold *et al.* (2002) and Ha *et al.* (2001) that use the initial radius to calculate the force per unit volume  $f_i$ . The current configuration  $f_i = \rho\omega^2(r + u)$  would be necessary for a more exact calculation.

The computation of  $\Delta W$  will consider the centrifugal force and the mentioned  $\Delta u$  with its sign, Fig. 8 left. The crack will grow uncontrollably if the increase in energy per unit area  $A$  released by this crack is more significant than the material's toughness. The total released energy  $U_R$  and the energy release rate  $G$  can be formulated as

$$U_R = -\Delta U + \Delta W; \quad G = \frac{dU_R}{dA} = \frac{1}{2\pi r_c} \frac{dU_R}{dz} \quad (1)$$

For the three stress-uniform cylinders, these energies are constant with  $z$ , so from now values per unit length with subscript  $l$  will be used instead of per unit area; the energy released is then

$$U_{Rl} = \frac{dU_R}{dz} \quad (2)$$

## 6. Increment of energy

The internal energy per unit volume of a general solid can be calculated with the scalar product of the stress and strain tensors, in Voigt notation

$$U_0 = \frac{\boldsymbol{\sigma} \cdot \boldsymbol{\epsilon}}{2} = \frac{\sigma_\theta \epsilon_\theta + \sigma_r \epsilon_r + \sigma_z \epsilon_z + \tau_{r\theta} \gamma_{r\theta} + \tau_{rz} \gamma_{rz} + \tau_{\theta z} \gamma_{\theta z}}{2} \quad (3)$$

Some terms in the right fraction can be simplified for the uniform cylinder: the axisymmetry cancels the fourth term since the shear deformation is null, and the almost uniform stresses in  $z$  cancel the fifth and sixth terms to the nullity of the related shear strains. Finally, the axial strain  $\epsilon_z^u$  is constant; see Koch *et al.* (2018). Applying the kinematic relations for small deformation in polar coordinates

$$U_0 = \frac{1}{2} \left( \sigma_\theta \frac{u}{r} + \sigma_r u_{,r} + \sigma_z \epsilon_z^u \right) \quad (4)$$

The total energy per unit crack length ( $dz \equiv 1$ ) of a cylinder with axisymmetric geometry will be noted again with the subindex  $l$ . Considering the differential of volume  $d\Omega = r d\theta dr \cdot 1$

$$U_l = \int_{\Omega} U_0 d\Omega = 2\pi \int_{r_i}^{r_e} U_0 r dr = \pi \int_{r_i}^{r_e} \sigma_{\theta} u dr + \pi \int_{r_i}^{r_e} r \sigma_r u_{,r} dr + \pi \epsilon_z^u \int_{r_i}^{r_e} r \sigma_z dr \quad (5)$$

$$:= U_{\theta l} + U_{r l} + U_{z l}$$

From Pérez-Aparicio and Ripoll (2011) and excluding the residual terms, each variable in the kernels can be expressed as

$$u = Ar^{-k} + Br^k + U_b r^3 + U_d r; \quad \sigma_{\theta} = H_A r^{-(k+1)} + H_B r^{k-1} + H_b r^2 + H_d \quad (6)$$

$$\sigma_r = R_A r^{k+1} + R_B r^{k-1} + R_b r^2 + R_d; \quad \sigma_z = \nu_{\theta z} \sigma_{\theta} + \nu_{r z} \sigma_r + E_z \epsilon_z^u$$

The terms  $A, B$  in the first expression are calculated from the internal and external boundary condition and continuity between adjacent layers; then, they have different values for each of the three cylinders (1), (2), or (3). Also, the coefficients  $U_b$  are a function of the centrifugal force and  $U_d$  of the internal axial force.

The parameter  $k$  represents the anisotropy of the material so that for an isotropic layer,  $k = 1$ . All the other parameters directly depend on the composite material, some in addition to the centrifugal and axial forces defined in the Appendix. Calculating the first integral of the middle Eq. (5) by substitution of the first and second Eq. (6), in each subcylinder of thickness  $r_{ij} - r_{ej}$  (where  $j = (1), (2), (3)$ ), the energy produced by the hoop stress is

$$U_{\theta l} = \pi \left[ AH_A \left( \frac{Ar^{-2k}}{-2k} + B \ln r + \frac{U_b r^{-k+3}}{-k+3} + \frac{U_d r^{-k+1}}{-k+1} \right) + \right. \\ BH_B \left( \frac{Br^{2k}}{2k} + A \ln r + \frac{U_b r^{k+3}}{k+3} + \frac{U_d r^{k+1}}{k+1} \right) + \\ H_b \left( \frac{U_b r^6}{6} + \frac{U_d r^4}{4} + \frac{Ar^{-k+3}}{-k+3} + \frac{Br^{k+3}}{k+3} \right) + \\ \left. H_d \left( \frac{U_b r^4}{4} + \frac{U_d r^2}{2} + \frac{Ar^{-k+1}}{-k+1} + \frac{Br^{k+1}}{k+1} \right) \right]_{r_{ij}}^{r_{ej}} \quad (7)$$

where it has been considered that the opening  $c$  (Fig. 5) is very small with respect to the radii. The integral solution is straightforward since it only involves simple exponentials of  $r$ . Similarly, the second integral of Eq. (5) transforms into

$$U_{r l} = \pi \left[ AR_A \left( \frac{Ar^{-2k}}{2} + kB \ln r + \frac{3U_b r^{-k+3}}{-k+3} + \frac{U_d r^{-k+1}}{-k+1} \right) + \right. \\ BR_B \left( -\frac{Br^{2k}}{2} - kA \ln r + \frac{3U_b r^{k+3}}{k+3} + \frac{U_d r^{k+1}}{k+1} \right) + \\ R_b \left( \frac{3U_b r^6}{6} + \frac{U_d r^4}{4} - \frac{kAr^{-k+3}}{-k+3} + \frac{kBr^{k+3}}{k+3} \right) + \\ \left. R_d \left( \frac{3U_b r^4}{4} + \frac{U_d r^2}{2} - \frac{kAr^{-k+1}}{-k+1} + \frac{kBr^{k+1}}{k+1} \right) \right]_{r_{ij}}^{r_{ej}} \quad (8)$$

Finally, the third integral related to the axial force energy is

$$U_{zl} = \pi \epsilon_z^u \left[ (v_{\theta z} H_A + v_{rz} R_A) \frac{Ar^{-k+1}}{-k+1} + (v_{\theta z} H_B + v_{rz} R_B) \frac{Br^{k+1}}{k+1} + (v_{\theta z} H_b + v_{rz} R_b) \frac{r^4}{4} + (v_{\theta z} H_d + v_{rz} R_d + E_z \epsilon_z^u) \frac{r^2}{2} \right]_{r_{ij}}^{r_{ej}} \quad (9)$$

For each subcylinder, the energies of Eqs. (7), (8), and (9) must be summed up. The increment of unit internal energy of the flywheel is

$$\Delta U_l = U_{l2} + U_{l3} - U_{l1} \quad (10)$$

The terms of the right-hand side correspond to the sum of Eq. (5) for each of the three cylinders. Notice that the energy of (2) and (3) is positive since their length increases with the crack, while that of (1) is negative due to its decrease, see Fig. 8.

## 7. Work of centrifugal force

All points inside the intact rotating flywheel are under a radial displacement field  $u(r, z)$  due to the centrifugal force; the crack's progression perturbs this initial field.

Since we assume that the infinitesimal displacement field does not change the centrifugal force, the work per unit volume  $W$  is proportional to only one difference between the initial  $u_{in}$  (intact) and final displacements  $u_{fi}$  (cracked). For a disk volume of unit length  $dz$ , we obtain  $W = f_i(u_{fi} - u_{in}) = f_i \Delta u$  and

$$W_l = \int_{\Omega} W \, d\Omega = 2\pi\rho\omega^2 \int_{r_i}^{r_e} (u_{fi} - u_{in}) r^2 \, dr \quad (11)$$

The situation for points with lower and greater radii than  $r_c$  will be studied separately. For the former, see Section 5,  $-\Delta u_2$  is the opposite of  $f_i$  generating a negative work. For the latter,  $\Delta u_3$  is in the sense of  $f_i$ , and therefore its work is positive.

$$\Delta W_2 = 2\pi\rho\omega^2 \int_{r_i}^{r_c} -\Delta u_2 r^2 \, dr; \quad \Delta W_3 = 2\pi\rho\omega^2 \int_{r_c}^{r_e} \Delta u_3 r^2 \, dr \quad (12)$$

The points in (1) do not significantly change their radial displacement, then  $\Delta W_1 = 0$ .

## 8. Fracture of a CFRP flywheel

Before the presentation of the main case, a previous consideration is made. Although it has been assumed that the crack is situated in the radial middle, the formulation accepts any position for simplicity. To check the influence of  $r_c$  in the results, in Fig. 9, the ratio between the calculated energy Eq. (5) for several crack radii and the maximum of the series is plotted. As expected, the energy is very low when the crack is close to the internal or external radii. This is due to the reduction of one of the subcylinders and consequently  $\Delta u \rightarrow 0$  in the other. For the dimensions given in Section 2, the highest ratio is 53% of the thickness for the first case and 57% for a thicker

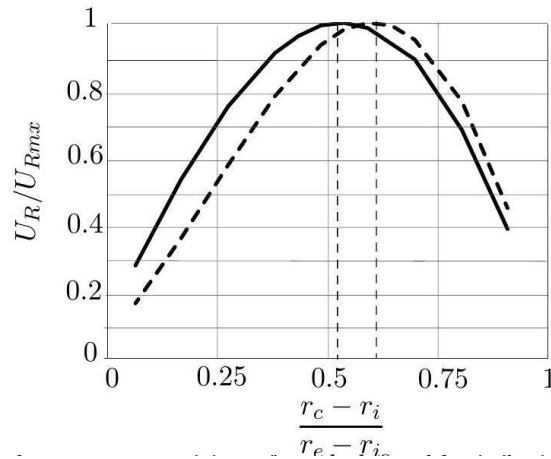


Fig. 9 Normalized released energy vs. position of crack defined by inflexion point. Continuous line  $r_e = 0.2$ , dashed line  $r_e = 0.3$  both with  $r_i = 0.1$  [m]

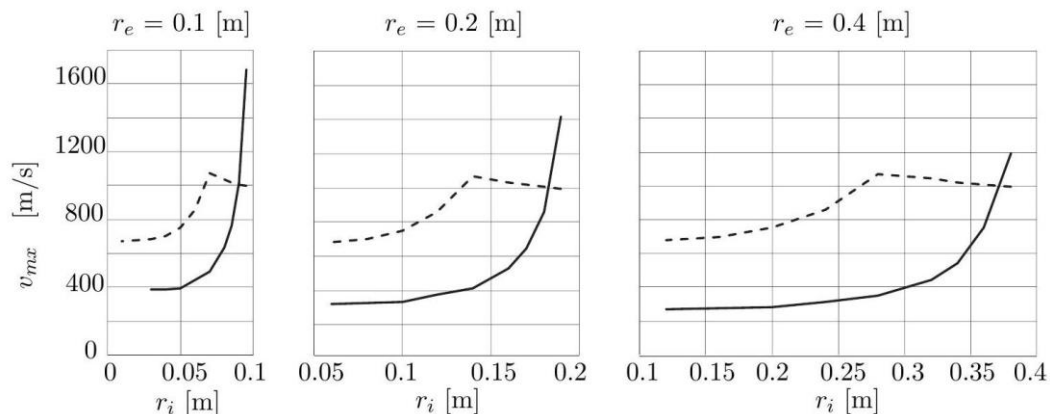


Fig. 10 Peripheral speed limits at  $r_e$  for failure of cylinders using stresses plus failure criterion (dashed line), and using fracture with the present study (continuous line) with the same external radius, several inner radii and common length  $L = 0.4$  [m]

flywheel. These peaks indicate the position in which the crack most likely will develop. In any case, the error in the final result of Fig. 10 is less than 5% when the crack is calculated in the middle.

The fracture of several flywheels made out of a single layer is analyzed in the following; the relevant material properties are listed in Table 1. Although in Section 3, it was justified that the fracture toughness of a unidirectional cylinder does not coincide with the interlaminar  $G_{r+}$  measured from a flat specimen (see Fig. 4), to the best of our knowledge no other information is available; therefore, the value of  $0.62$  [kJ/m] will be used.

A parametric study for cylinders of several internal and external radii is now presented in Fig. 10, fixing  $r_e$  in each figure and varying  $r_i$  nine times; for each of the 27 cases, the maximum linear velocity at  $r_e$  (proportional to  $\omega$ , see Fig. 3) that produces sudden propagation of the crack is solved by iteration of  $b$  in the first equation of the Appendix--the initiation is taken for sure

starting at minor defects--. Therefore, these values are the limit of revolutions before the flywheel breaks.

Alternatively, with the geometry of each case, all stresses are calculated with the formulae from Pérez-Aparicio and Ripoll (2003), and with the criterion of Christensen (1997), a new peripheral velocity  $v$  is again solved by iteration. This approach does not consider Fracture theory but Strength of Materials theory, that is, failure by stress limit. The reason for choosing this criterion is that it is especially suitable for very thick composite laminates.

The discontinuity in the dashed lines of Fig. 10 represents two different failure modes: according to Christensen (1997), for relatively thick-wall flywheels the matrix is damaged. Although the failure criteria cannot consider fracture, the situation corresponds to that of a  $\theta - z$  (Fig. 1) crack, as the one analyzed in the present work. For relatively thin-wall flywheels, the crack would be in the  $r - z$  plane, with a total loss of structural integrity and a catastrophic failure. With the matrix failure mode, the initial cylinder is divided into two concentric ones of the thinner wall, in theory, with better progressive failure resistance.

## 9. Conclusions

A cylindrical flywheel with an initial crack in the circumferential-axial plane that extends the complete perimeter will generally present a fracture limit at a lower speed than the predicted from a failure criterion; this difference means that for the design of real flywheels, the former approach must be applied. The evolution of these fracture results is exponential, implying that thin rotors are relatively immune to crack propagation but that thick ones are very prone. This incremental response is more relevant when the external diameter is small. The failure criterion predicts an increment of speed limit with the reduction of thickness, but at a certain  $r_i$ , the limit decreases; the reason is that for a particular ratio  $r_e/r_i$  when the cylinder becomes thin, the level of the radial stress  $\sigma_r$  is low and  $\sigma_\theta$  becomes prevalent--although  $\sigma_\theta/X_{1+}$  is always relatively small due to the high strength in this direction--. That is, the failure mechanism changes from matrix failure to fiber failure.

## References

- Arnold, S.M., Saleeb, A.F. and Al-Zoubi, N.R. (2002), "Deformation and life analysis of composites flywheel disk systems", *Compos.: Part B*, **33**, 433-459. [https://doi.org/10.1016/S1359-8368\(02\)00032-X](https://doi.org/10.1016/S1359-8368(02)00032-X).
- Cepero, F., García, I., Justo, J., Mantic, V. and París, F. (2019), "An experimental study of the translaminar fracture toughnesses in composites for different crack growth directions, parallel and transverse to the fiber direction", *Compos. Sci. Technol.*, **181**, 107679. <https://doi.org/10.1016/j.compscitech.2019.107679>.
- Christensen, R.M. (1997), "Stress based yield/failure criteria for fiber composites", *Int. J. Solid. Struct.*, **34**(5), 529-543. [https://doi.org/10.1016/S0020-7683\(96\)00038-8](https://doi.org/10.1016/S0020-7683(96)00038-8).
- El-Hajjar, R. and Haj-Ali, R. (2005), "Mode-I fracture toughness testing of thick section FRP composites using the ESE ( $T$ ) specimen", *Eng. Fract. Mech.*, **72**(4), 631-643. <https://doi.org/10.1016/j.engfracmech.2004.03.013>.
- González, E.V., Maimí, P., Martín-Santos, E., Soto, A., Cruz, P., Martín-Escalera, F. and Sainz-Aja, J.R. (2018), "Simulating drop-weight impact and compression after impact tests on composite laminates using conventional shell finite elements", *Int. J. Solid. Struct.*, **144-145**, 230-247. <https://doi.org/10.1016/j.ijsolstr.2018.05.005>.

- Ha, S.K., Yang, H.I. and Kim, D.J. (2001), "Optimum design multi-ring composite flywheel rotor using modified generalized plane strain assumption", *Int. J. Mech. Sci.*, **43**, 993-1007. [https://doi.org/10.1016/S0020-7403\(00\)00047-3](https://doi.org/10.1016/S0020-7403(00)00047-3).
- Haj-Ali, R., El-Hajjar, R. and Muliana, A. (2006), "Cohesive fracture modeling of crack growth in thick-section composites", *Eng. Fract. Mech.*, **73**(15), 2192-2209. <https://doi.org/10.1016/j.engfracmech.2006.04.003>.
- Ibrahimbegovic, A. and Mejia-Nava, R.A. (2021), "Heterogeneities and material scales providing physically-based damping to replace Rayleigh damping for any structure size", *Couple. Syst. Mech.*, **10**(3), 201-216. <https://doi.org/10.12989/csm.2021.10.3.201>.
- Ibrahimbegovic, A., Matthies, H.G., Dobrilla, S., Karavelić, E., Nava, R.A.M., Nguyen, C.U., ... & Vondřejc, J. (2022), "Synergy of stochastics and inelasticity at multiple scales: Novel Bayesian applications in stochastic upscaling and fracture size and scale effects", *SN Appl. Sci.*, **4**(7), 191. <https://doi.org/10.1007/s42452-022-04935-y>.
- Koch, I., Just, G., Otrembab, F., Berner, M. and Gude, M. (2018), "Analysis of the micro-cracking behavior of carbon fibre reinforced flywheel T rotors considering residual stresses", *Compos. Struct.*, **204**, 587593. <https://doi.org/10.1016/j.compstruct.2018.07.130>.
- Lenz, J., Blackman, B.R.K., Taylor, A.C., Morgan, R. and Crua, C. (2014), "Selection of test methods to examine the fracture mechanics of carbon fibre composite flywheels", *16th European Conf. on Composite Materials*, January.
- Nguyen, C.U., Hoang, T.V., Hadzalic, E., Dobrilla, S., Matthies, H.G. and Ibrahimbegovic, A. (2022), "Viscoplasticity model stochastic parameter identification: Multi-scale approach and Bayesian inference", *Couple. Syst. Mech.*, **11**(5), 411-442. <https://doi.org/10.12989/csm.2022.11.5.411>.
- Pérez-Aparicio, J.L. and Ripoll, L.I. (2003), "Solución generalizada para piezas cilíndricas de material compuesto", *Proceedings V Congreso AEMAC*, Zaragoza, July.
- Pérez-Aparicio, J.L. and Ripoll, L.I. (2011), "Exact, integrated and complete solutions for composite flywheels", *Compos. Struct.*, **93**, 1404-1415. <https://doi.org/10.1016/j.compstruct.2010.11.011>.
- Rizov, V. (2020), "Investigation of two parallel lengthwise cracks in an inhomogeneous beam of varying thickness", *Couple. Syst. Mech.*, **9**(4), 381-396. <https://doi.org/10.12989/csm.2020.9.4.381>.
- Suljevic, S., Ibrahimbegovic, A., Karavelic, E. and Dolarevic, E. (2022), "Meso-scale based parameter identification for 3D concrete plasticity model", *Couple. Syst. Mech.*, **11**(1), 55-78. <https://doi.org/10.12989/csm.2022.11.1.055>.
- Taylor, R.L. and Govindjee, S. (2020), "FEAP a finite element analysis program", Programmer Manual, University of California, Berkeley.
- Tzeng, J.T. (1998), "Dynamic response and fracture of composite cylinders", *Compos. Sci. Technol.*, **58**, 1443-1451. [https://doi.org/10.1016/S0266-3538\(98\)00021-9](https://doi.org/10.1016/S0266-3538(98)00021-9).
- Tzeng, J.T. and Moy, P. (2008), "Composite energy storage flywheel design for fatigue crack resistance", *14th Symposium on Electromagnetic Launch Technology*, June.
- Tzeng, J.T. and Pipes, R.B. (1992), "Thermal and residual stress analysis for in-situ and post consolidated composites ring", *Compos. Manuf.*, **3**, 273-279. [https://doi.org/10.1016/0956-7143\(92\)90114-A](https://doi.org/10.1016/0956-7143(92)90114-A).
- Tzeng, J.T., Emerson, R. and Moy, P. (2006), "Composite flywheels for energy storage", *Compos. Sci. Technol.*, **66**, 2520-2527. <https://doi.org/10.1016/j.compscitech.2006.01.025>.
- Wang, Y., Xingjia, D., Kunpeng, W. and Xingfeng, G. (2018), "Progressive failure behavior of composite flywheels stacked from annular plain profiling woven fabric for energy storage", *Compos. Struct.*, **194**, 377-387. <https://doi.org/10.1016/j.compstruct.2018.04.036>.
- Wang, Y., Yu, B., Ji, K., Chen, J. and Zhaoyang, W. (2020), "Research on crack expansion characteristics of semi-disc polymethyl methacrylate specimen with weak prefabricated double-layer surfaces under dynamic load", *Eng. Fract. Mech.*, **235**, 107170. <https://doi.org/10.1016/j.engfracmech.2020.107170>.

## Appendix

The inertial and axial deformations are defined only by two respective coefficients:

$$b = -\frac{\rho\omega^2}{p}; \quad d = (k^2n_H - n_R)\varepsilon_z^u$$

$$U_b = \frac{b}{9 - k^2}; \quad U_d = \frac{d}{1 - k^2}$$

expressions that include the following material coefficients related to transversal isotropy,  $\nu_{\theta z} = \nu_{r\theta}$  and  $E_r = E_z$ :

$$s_{11} = \frac{1 - \nu_{\theta z}^2}{E_\theta}; \quad s_{12} = \nu_{\theta z} \frac{1 + \nu_{rz}}{E_r}$$

$$s_{21} = s_{12}; \quad s_{22} = \frac{1 - \nu_{rz}^2}{E_r}$$

$$\nu_H = \frac{s_{12}}{s_{22}}; \quad \nu_R = \frac{s_{12}}{s_{11}}$$

$$n_H = \nu_{\theta z} + \nu_H \nu_{rz}; \quad n_R = \nu_R \nu_{\theta z} + \nu_{rz}$$

$$k^2 = \frac{s_{22}}{s_{11}}; \quad p = \frac{s_{11}}{s_{11}s_{22} - s_{12}^2}$$

At Eq. (6), the stress coefficients associated only with material properties are:

$$H_A = k^2p(1 - k\nu_H); \quad H_B = k^2p(1 + k\nu_H)$$

$$R_A = p(\nu_R - k); \quad R_B = p(\nu_R + k)$$

From the same equation, the stress coefficients that include material, centrifugal, and axial behavior are:

$$H_b = k^2p(1 + 3\nu_H)U_b; \quad H_d = k^2p(1 + \nu_H)U_d + n_H\varepsilon_z^u$$

$$R_b = p(3 + \nu_R)U_b; \quad R_d = p[(\nu_R + 1)U_d + n_R\varepsilon_z^u]$$